

# An End-to-End Physics-Informed Neural Network for Defect Identification and 3-D Reconstruction Using Rotating Alternating Current Field Measurement

Jianming Zhao , Wei Li , Member, IEEE, Xin'an Yuan , Xiaokang Yin , Senior Member, IEEE, Xiao Li , Qinyu Chen , and Jianxi Ding

**Abstract**—The alternating current field measurement (ACFM) technique has been widely used in the defect detection of metal structures. However, the identification and reconstruction of defects depend on human experience or simple empirical formulas, which leads to misjudgment of defects and large quantization errors. In this article, we propose an end-to-end physics-informed neural network for defect identification and 3-D reconstruction. The high-precision automatic detection system with a specially designed probe is established to detect defects in any direction. The faster RCNN network is used to identify and classify defects. The physics-informed Pix2Pix network is constructed to realize 3-D reconstruction of defects with different types. The results show that the established end-to-end physics-informed neural network can realize the identification and 3-D reconstruction of defects in which the mean average precision is 0.9982, the average length error of cracks is 0.9249 mm, the average depth error of cracks is 0.3402 mm, the average volume error of corrosion is 0.0667, and the average maximum depth error of corrosion is 0.3464 mm.

**Index Terms**—Alternating current field measurement (ACFM), defect 3-D reconstruction, defect identification and classification, end-to-end physics-informed neural network.

## I. INTRODUCTION

NONDESTRUCTIVE testing (NDT) technologies aim to evaluate the location, size, type, quantity, and other information of defects in the tested object without affecting the tested material or system structure state and performance. NDT

Manuscript received 26 July 2022; revised 9 October 2022; accepted 22 October 2022. Date of publication 28 October 2022; date of current version 20 June 2023. This work was supported in part by the National Natural Science Foundation of China under Grant 52275556 and Grant 52005512 and in part by the Fundamental Research Funds for the Central Universities under Grant 22CX01003A-5. Paper no. TII-22-3248. (Corresponding authors: Wei Li; Xin'an Yuan.)

The authors are with the Center for Offshore Engineering and Safety Technology, China University of Petroleum (East China), Qingdao 266580, China (e-mail: jianmingzhao123@163.com; liwei@upc.edu.cn; xinancom@163.com; xiaokang.yin@upc.edu.cn; lix2020@upc.edu.cn; chenqy0802@163.com; dingjianxi102@163.com).

Color versions of one or more figures in this article are available at <https://doi.org/10.1109/TII.2022.3217820>.

Digital Object Identifier 10.1109/TII.2022.3217820

is widely used in various fields, such as shipbuilding, aerospace, nuclear energy, and railways, which has become an indispensable method to ensure product quality and safe operation of equipment [1]. The traditional NDT techniques mainly include magnetic particle testing (MT), penetration testing (PT), ultrasonic testing (UT), magnetic flux leakage (MFL), visual testing (VT), and eddy current testing (ECT). MT and PT are effective in detecting surface defects, but the depth information cannot be obtained [2]. UT has high detection sensitivity for buried defects [3]. And MFL is one of the most widely used technique for defect detection in ferromagnetic materials [4]. The traditional VT techniques include endoscopic NDT, infrared thermography, terahertz imaging, etc., which are intuitive and efficient due to the identification of defects by images [5], [6], [7]. And the latest VT techniques often combine with other NDT techniques. ECT and infrared thermography were combined to improve the accuracy of detection [8]. For rapid optical detection of defects, magnetic nanoemulsion thin film sensors were used in MFL [9]. But the VT is not accurate for defect depth measurement. ECT is widely used for surface defect detection in metallic materials because of its characteristics of low cost, fast imaging, and high resolution. However, it requires a thorough cleaning of the inspected structure surface and is sensitive to lift-off [10].

Alternating current field measurement (ACFM) is an important electromagnetic NDT method, which combines the uniform current of alternating current potential drop testing technology and the noncontact characteristics of ECT. Due to the advantages of quantitative evaluation and insensitivity to lift-off, ACFM technique has been used in many industrial fields, such as nuclear power, rail transportation, and aerospace [11]. At present, the research on ACFM is mainly divided into two aspects: one is the research on excitation methods, and the other is the research on characteristic signal processing methods.

The excitation method of classic ACFM is realized by winding coils on a U-shaped magnetic core. The detection coil is used to collect the magnetic field signal, and the defect is determined by the voltage signal collected in the detection coil. The classic form of the detection probe is widely used to inspect various structures, such as rails and wheels [12], and welds [13]. However, the traditional detection probes use a single coil

to induce the electromagnetic field, and it is more sensitive to cracks perpendicular to the induced current than those at other angles. In order to overcome this shortcoming, rotating alternating current field measurement (RACFM) was proposed, which uses two or more coils to induce a rotating uniform electromagnetic field. Li et al. [14] proposed a double U-shaped orthogonal inducer for arbitrary-angle underwater cracks. Zhang et al. [15] developed a probe with three-phase excitation and integrated array tunnel magnetoresistance sensors to recognize a small defect in different directions. Ye et al. [16] used a probe with three-phase coils to detect axial and circumferential notches in steam generator tubes in nuclear power plants. An encircled probe with six excitation windings was constructed and used to inspect a steel pipe with axial and circumferential defects [17]. It can be seen that the excitation mode plays a decisive role in the detection sensitivity of defects at different angles.

For characteristic signal processing methods, the main goal is to achieve defect identification and quantification. First, the current defect identification methods mainly make defect signal features easier to identify by improving the signal-to-noise ratio, such as signal gradient algorithm [18], tradeoff denoising algorithm [19], and then realize defect judgment by designing thresholds or signal features. Second, the quantification of defects is mainly divided into two stages according to the degree of realization. The first stage is that only the sizes of the defect are obtained, such as the length and depth of the crack. And the second stage is that the defect contour is reconstructed. For the quantification of the defect size, the implementation of the algorithms is generally divided into two steps. The first step is to establish a dataset between the eigenvalues of the signal and the defect size, and the second step is that the sizes of the defect are obtained by interpolation [20], [21], simple machine learning network [22], etc. In order to realize the reconstruction of the defect contour, the mapping relationship between the complete feature signal and the defect contour needs to be established. Pasadas et al. [23], [24] proposed a Tikhonov regularized inversion algorithm to obtain the 2-D surface defect images. Yuan et al. [25] developed the gradient imaging algorithm to show visual morphology of defects with different types. Noroozi et al. [26] implemented the reconstruction of the crack profiles by the fuzzy learning approach. But the above algorithms are only applicable to the reconstruction of the profiles or surface of the defect. In conclusion, there are three main problems in the identification and quantification of defects. First, the traditional ACFM defect identification method relies on personnel experience, which is inefficient and prone to misjudgment of defects. Second, the defect quantification method needs to establish the relationship between the original signal characteristic value and the defect size, which leads to a smaller application range due to the different characteristics for different types of defects. The third problem is that the methods of defect contour reconstruction are all 2-D. But the 3-D profile is more valuable for structural safety assessment because it can get both surface and depth information.

With the development of deep learning technology, more and more industries have used its excellent learning ability to solve complex feature extraction, nonlinear mapping, and other

difficult problems. In the field of electromagnetic NDT, apart from a few studies that use deep learning networks to identify and classify defects [27], [28], there are few related works that solve the nonlinear mapping relationship between magnetic field images and defect 3-D contours. However, combining the advantages of deep learning with RACFM characteristic signals has great application potential in solving the problems of misjudgment of defects, large quantization errors, and low efficiency in the NDT field.

This article provided an effective method for the intelligent identification, 3-D reconstruction, and accurate evaluation of various surface defects in the metallic materials using RACFM technique, as shown in Fig. 1. To achieve automatic scanning and high-precision localization, a collaborative detection system of robot and RACFM system was established. To achieve the identification and 3-D reconstruction of defects with different types, an end-to-end physics-informed neural network was established, which consists of a faster-RCNN network and a physics-informed Pix2Pix network embedded with quantitative indicators of defects.

The rest of this article is organized as follows. The detection system and probe are developed in Section II. The intelligent identification and classification method for surface defects of metal structures is established in Section III. The defect 3-D reconstruction algorithm is built based on a physics-informed Pix2Pix network in Section IV. Finally, Section V concludes this article.

## II. DETECTION SYSTEM SETUP

### A. Simulation Analysis of Probe With Different Excitation Coils

The excitation mode is the core of the detection probe. To optimize the combination scheme of the excitation coils and realize the detection of defects in any direction, different excitation modes are analyzed and compared. The finite-element method (FEM) models containing one coil, two coils, and three coils are established, respectively. The simulation model containing three coils is shown in Fig. 2. The one coil is composed of two completely symmetrical rectangular coils, the two coils are orthogonally distributed, and the angle between each coil of the three coils is 120°. The currents in the excitation coils are written as follows:

$$I_1 = I_0 \sin(\omega t) \quad (1)$$

$$\begin{bmatrix} I_1 \\ I_2 \end{bmatrix} = I_0 \begin{bmatrix} \sin(\omega t) \\ \sin(\omega t + \pi/2) \end{bmatrix} \quad (2)$$

$$\begin{bmatrix} I_1 \\ I_2 \\ I_3 \end{bmatrix} = I_0 \begin{bmatrix} \sin(\omega t) \\ \sin(\omega t + \pi/3) \\ \sin(\omega t + 2\pi/3) \end{bmatrix} \quad (3)$$

where  $I_0$  indicates the amplitude of the current and  $\omega$  is the angular frequency. The current amplitude is set to 0.3 A and the frequency is set to 1 kHz in the FEM models.

To analyze the variation law of the induced current under different excitation coils, time-domain analysis is set in the model. And a polar plot of the total induced current magnitude

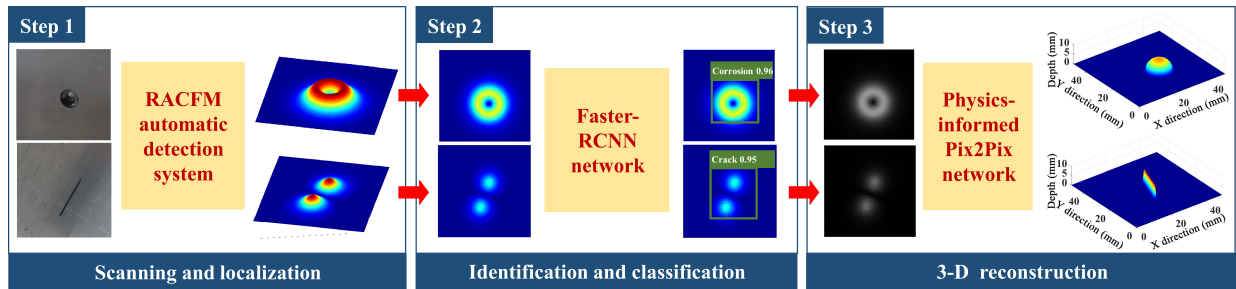


Fig. 1. Flowchart of the proposed method.

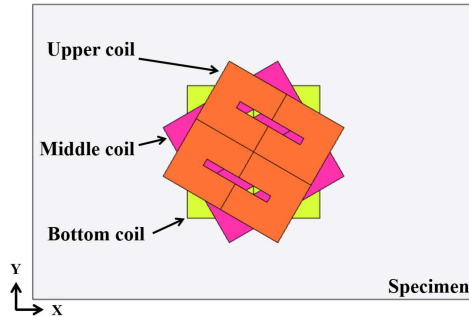


Fig. 2. Three-dimensional FEM model.

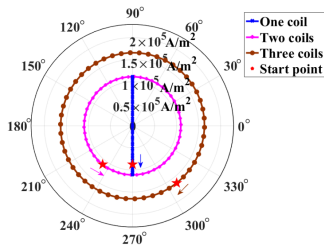


Fig. 3. Magnitude and angle of the total induced current.

and angle for one cycle is shown in Fig. 3. It indicates that the angle of the total induced current generated by the model with one coil is only 90° and 270°, and the amplitude is variable. So, it is not sensitive to the defects parallel to the induced current. The models with two and three coils can generate induced currents with constant amplitude and periodic changes in angle, which indicate that both excitation methods can overcome the directional problem of the traditional ACFM technology. The difference is that the initial angle of the total induced current is different and the amplitude of the three coils is larger, which is the effect of superposition of the induced currents of multiple coils. The total induced currents rotate in the opposite directions, one clockwise and the other counterclockwise. However, these differences have no effect on sensitivity.

The distribution of the total induced current is an important factor in the fabrication of the probe. The frequency analysis is set up in the simulation model and the surface-induced current density is extracted, as shown in Fig. 4. The uniform induced current of one coil is mainly concentrated in the middle of the coil, which is also the utilization area of the probe. The utilization areas for two and three coils are overlapping areas in the middle

of the coils. The overlapping area of the two coils is close to a square and that of the three coils is close to a circle, which is the result of the superposition of multiple coils. Therefore, when the number of excitation coils increases, the overlapping area will become smaller, which is not conducive to detecting defects.

### B. Probe Experimental Testing

To verify the results in the simulation, probes with different excitation coils are established. As shown in Fig. 5, the detection probe is mainly composed of excitation coils, the magnetic sensor, and the amplification filter circuit. The magnetic sensor is the commercial TMR packages type 2301 from Duowei in China. The coil is made of a printed circuit board (PCB) board. One coil consists of two symmetrically distributed rectangular coils. The number of turns of the rectangular coil is 50, the wire diameter is 0.2 mm, and the wire spacing is 0.15 mm. The two coils and the three coils are, respectively, made of multilayer PCB boards. The arrangement of the two coils and three coils is the same as in the simulation. The frequency and amplitude of the excitation signal are the same as in the simulation.

Since the  $B_z$  (the magnetic flux density in the direction perpendicular to the scanning surface) signal is generated by the disturbance of the induced current, and the maximum distortion is at the endpoint of the crack, the probes sweep the endpoints of the different angles' cracks (0°, 30°, 45°, 60°, and 90°). The test results under different excitation coils are shown in Fig. 6. The results show that, for one coil, the distortion value of the  $B_z$  signal is the largest when the crack angle is 0°. With the increase of the crack angle, the distortion value of the  $B_z$  signal gradually becomes smaller. When the crack is 90°, the defect cannot be identified. Unlike the single coil model, the  $B_z$  signal distortion values of the models with two and three coils do not decrease with the increase of the crack angle. For cracks at any angle, the value of distortion is almost unchanged. The base and distortion values of the  $B_z$  signal of the three-coil model are larger than those of the two-coil model, which is verified in the simulation. But this is not critical as it can be achieved by increasing the current amplitude of the excitation signal.

In conclusion, both the probes with two and three coils have the same sensitivity to defects in any direction, but the overlapping area of the three coils is smaller, and it also increases the complexity of the system. For example, the lift-off heights of different coils are not exactly the same, which increases the

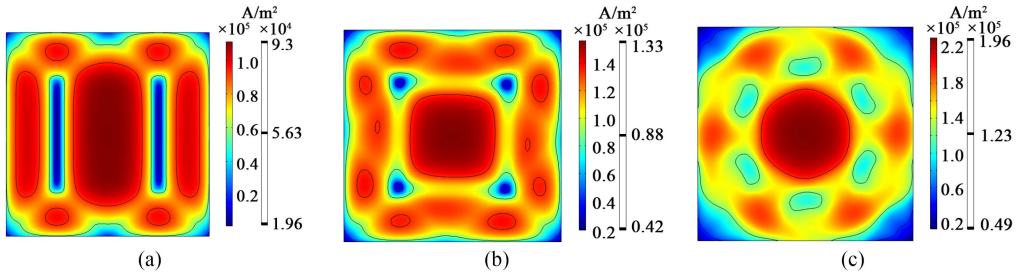


Fig. 4. Surface-induced current distribution. (a) One coil. (b) Two coils. (c) Three coils.

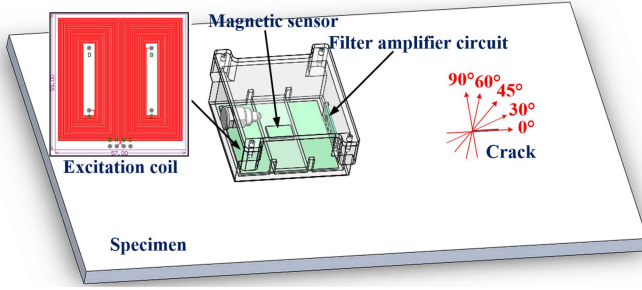


Fig. 5. Schematic diagram of the probe.

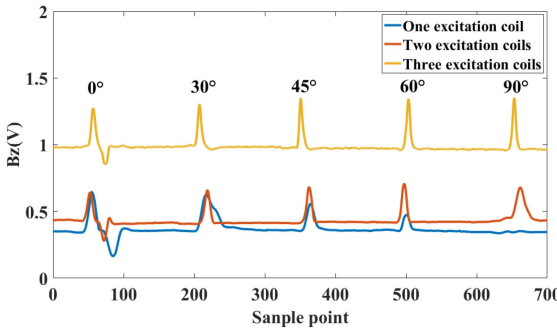


Fig. 6. Different angle crack detection results of the different probes.

measurement error. Therefore, the probe in this article adopts two coils.

### C. High-Precision Automatic Detection System Setup

In order to achieve precise location and automatic detection of structural defects, a collaborative detection system in which a robot and RACFM system cooperate is established, as shown in Fig. 7. The automatic detection system mainly includes a robotic arm motion system, a RACFM system, and a collaborative detection software system. The robotic arm motion system is mainly composed of the manipulator, the motion controller, and the computer. The RACFM system is designed and developed independently, and mainly includes the detection probe, the power module, the signal generator, the power amplifier, the data acquisition card, and the computer. The computer and other components are integrated together for portability. The collaborative detection software is written based on Qt and C++, and it includes a robot control module, signal synchronization acquisition module, signal processing module, and display module. All

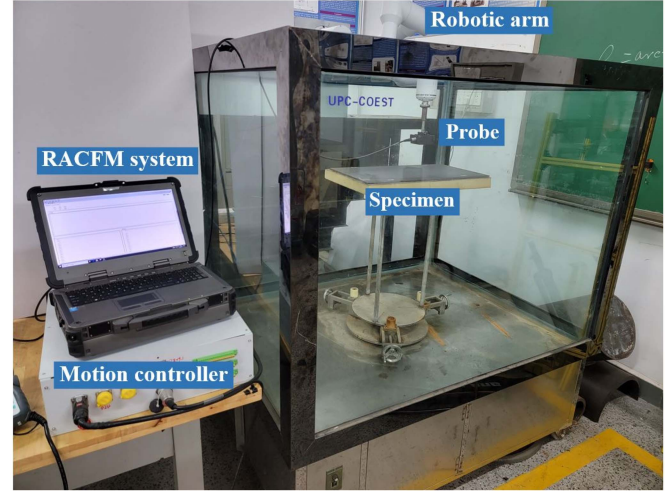


Fig. 7. High-precision automatic detection system.

the software are integrated into the RACFM detection system. The coordinate error of the automatic detection system is less than 0.1 mm.

## III. INTELLIGENT IDENTIFICATION OF DEFECTS

### A. Characteristic Image Analysis

In the NDT industry, defects are generally classified into two types: cracks and corrosion. They have different contours and evaluation indicators. Therefore, in this article, cracks at different angles and three typical corrosion are selected for identification and quantification.

First, the  $B_z$  image of cracks is analyzed. Cracks (length = 20 mm, width = 0.5 mm, and depth = 3 mm) with different angles ( $0^\circ$ ,  $30^\circ$ ,  $45^\circ$ ,  $60^\circ$ , and  $90^\circ$ ) are set in the simulation model, and the  $B_z$  images are shown in Fig. 8. At the position without a crack, the value of the  $B_z$  image is 0, and at the two endpoints of the crack, the  $B_z$  image shows two peaks. For cracks with different angles, the values of the two peaks are consistent, which also proves that the RACFM with two coils has the same sensitivity to cracks in any direction, and the angle between the two peaks is equal to the angle of the crack.

To analyze the  $B_z$  images of corrosion, rectangular, cylindrical, and spherical corosions are simulated, respectively, and their  $B_z$  images are obtained, as shown in Fig. 9. The corrosion contours and the distorted regions of the  $B_z$  images exhibit a

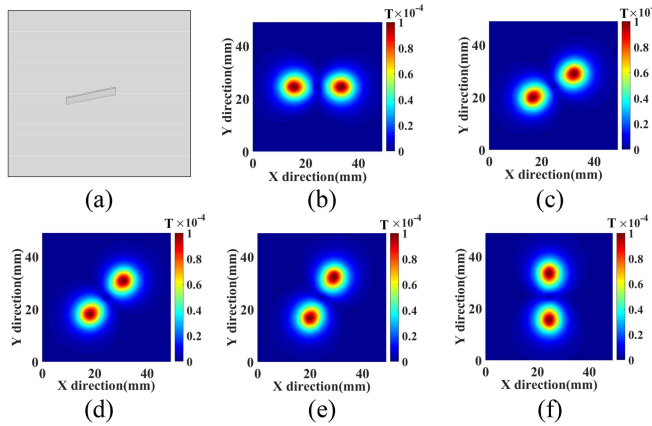


Fig. 8.  $B_z$  images of cracks at different angles. (a) Crack. (b)  $0^\circ$ . (c)  $30^\circ$ . (d)  $45^\circ$ . (e)  $60^\circ$ . (f)  $90^\circ$ .

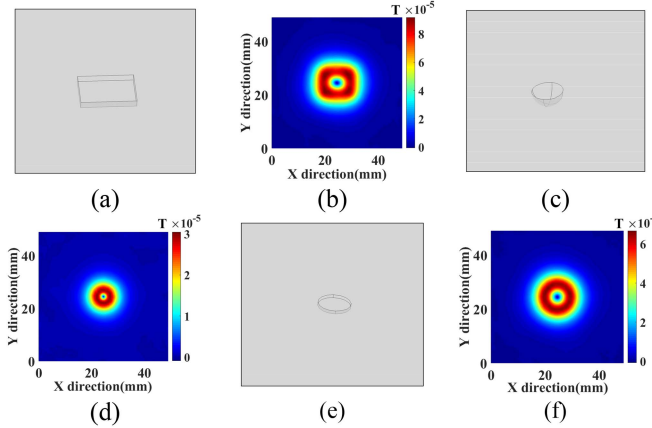


Fig. 9. Corrosion and  $B_z$  image. (a) Rectangular corrosion. (b)  $B_z$  image of rectangular corrosion. (c) Spherical corrosion. (d)  $B_z$  image of spherical corrosion. (e) Cylindrical corrosion. (f)  $B_z$  image of cylindrical corrosion.

certain shape correlation. At the outer edge of the corrosion, the value of the  $B_z$  signal is larger, and the value of the  $B_z$  signal gradually becomes smaller when it is close to the center point or away from the edge.

## B. Defect Identification and Classification Method

**1) Dataset Establishment:** In order to realize intelligent identification and classification of defects, an image dataset with various defects has been established. Due to the lack of defect data in the actual industry, we employ simulations and experiments to generate the  $B_z$  images with different defects. The simulation results are obtained through the simulation model in Section III, and the experimental results are obtained through the detection system established in Section II. There are 1290 image samples with two types of defects (645 samples with cracks and 645 samples with corrosion). There are 1030 simulated samples and 260 experimental samples. We adopt the commonly used pseudocolor in the electromagnetic NDT industry to generate the samples, as shown in Fig. 10. Because RACFM has the same detection sensitivity for defects in any direction, which

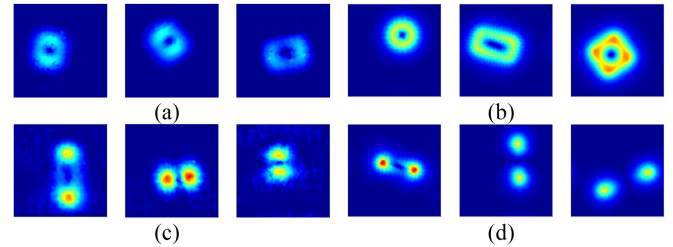


Fig. 10. Defect dataset. (a) Experimental corrosion. (b) Simulated corrosion. (c) Experimental cracks. (d) Simulated cracks.

TABLE I  
RESULTS OF DEFECT IDENTIFICATION AND CLASSIFICATION

Model	Corrosion			Crack			mAP
	Precision	Recall	AP	Precision	Recall	AP	
YOLOv7	1.0000	1.0000	1.0000	0.9826	0.9826	0.9819	0.9909
SSD	0.9931	1.0000	1.0000	0.9655	0.9739	0.9067	0.9534
Faster-RCNN	<b>0.9597</b>	<b>1.0000</b>	<b>0.9987</b>	<b>0.9664</b>	<b>1.0000</b>	<b>0.9977</b>	<b>0.9982</b>

is proved in Section III, the images are randomly rotated and moved to enrich the types. The maximum value of the colormap range is set at 1–3 times the maximum value of  $B_z$  image to obtain different color contrasts.

**2) Target Detection Algorithm:** At present, the detection algorithms based on deep learning are mainly divided into two categories, including two-stage methods and one-stage methods. The two-stage detection algorithm is a candidate region-based detection algorithm represented by the R-CNN series, and the single-stage detection algorithm is a regression analysis-based detection algorithm represented by YOLO and SSD. In order to get good results, this article uses YOLO v7 [29], SSD [30], and faster-RCNN [31] to localize and classify different types of defects, respectively. The entire dataset is divided into a training set, a test set, and a validation set at a ratio of 7:2:1. The epochs for all three models are set to 100. The confidence threshold is 0.4, and the Intersection over Union threshold is 0.6.

**3) Analysis of Test Results:** The performance of the target detection network is mainly evaluated by precision, recall, average precision (AP), mean average precision (mAP), and frame per second (FPS). Precision is the proportion of positive samples correctly predicted to positive classes of all predictions, and the calculation formula is as follows:

$$\text{Precision} = \frac{\text{TP}}{\text{TP} + \text{FP}} \quad (4)$$

where TP is a positive class predicted to be a positive class, and FP is a negative class predicted to be a positive class.

Recall is the ratio of correctly predicted positive samples to all true positive classes, and the calculation formula is as follows:

$$\text{Recall} = \frac{\text{TP}}{\text{TP} + \text{FN}} \quad (5)$$

where FN is a positive class predicted to be a negative class. The recognition results of different methods are shown in Table I. The recognition and classification results of the faster RCNN network are better than the other two. Its mAP is 0.9982, the

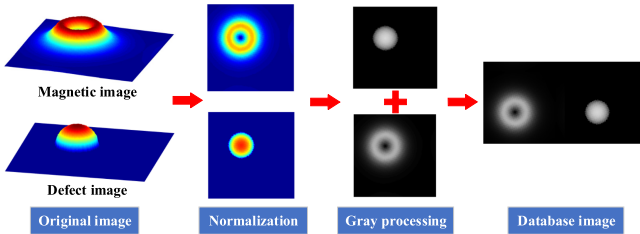


Fig. 11. Establishment process of the paired image.

AP for crack identification is 0.9977, and the AP for corrosion identification is 0.9987. Its crack and corrosion recognition precision are lower than the YOLO v7 networks, and the recall rates are both 1. This means that the network will not cause defects to be missed, but it is easy to identify nondefective areas as defective areas, which is acceptable and beneficial for device safety. For the evaluation index FPS, the network can identify 73 images/min in the RACFM detection instrument, which can fully meet the requirements of automatic detection system [CPU: Intel(R) Xeon(R) Gold 6226R, RAM(256 GB)]. In order to verify the generalization ability of the network, the samples in the validation set were identified. Precision is 0.9861 and recall is 1 for cracks. Precision is 0.9667 and recall is 1 for corrosion. It is proved that the network has good performance in identifying and classifying defects.

#### IV. THREE-DIMENSIONAL RECONSTRUCTION OF DEFECTS

##### A. Paired Image Dataset Establishment

The 3-D contour of the defect is very important for the safety assessment of the structure, but it is extremely difficult to solve the inverse problem from the magnetic field image to the 3-D contour of the defect due to the existence of nonunique solutions to the solving physical equations. Generative adversarial nets have shown excellent performance for solving the mapping problem of paired images. First, the dataset of paired  $B_z$  image and defect 3-D contour image needs to be established. The establishment process of paired image is shown in Fig. 11. The first step is to convert the  $B_z$  magnetic field signal into the  $B_z$  image of 100\*100 pixels, and the distance between each pixel is 0.5 mm. Then, a defect image is built according to the 3-D contour of the defect, and its size and distance between each pixel are consistent with the  $B_z$  image. The second step is the normalization process, and the normalized image is obtained via dividing by the maximum value of all images, where the simulated image is divided by  $3.5 \times 10^{-4}$  T, and the experimental image is divided by 0.95 V. The normalized defect image is obtained via dividing by 9 mm, which is the largest defect depth in the database. The third step is to convert the image to a grayscale image in order to reduce the amount of computation. In the fourth step, the  $B_z$  image and the corresponding defect image are formed into a paired image. Fig. 12 shows four different types of paired images. Different datasets are built, as shown in Table II. For the Cr dataset, there are 645 image samples of cracks. Among them, 600 samples (500 simulations, 100 experiments) are used for training, 30 samples are used for

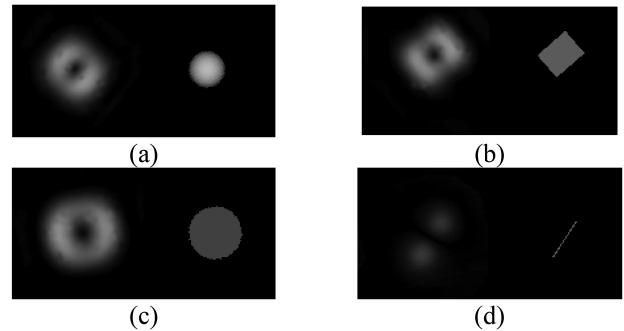


Fig. 12. Four different types of paired images. (a) Spherical corrosion. (b) Rectangular corrosion. (c) Cylindrical corrosion. (d) Crack.

TABLE II  
DATASETS WITH DIFFERENT TYPES OF DEFECTS

Dataset	Crack		Corrosion		Total
	Simulation	Experiment	Simulation	Experiment	
Cr	515	130	0	0	645
Co	0	0	515	130	645
To	515	130	515	130	1290

testing (15 simulations, 15 experiments), and 15 experimental samples are used for verification. The division ratio of Co and To datasets is the same as that of Cr.

##### B. Three-Dimensional Reconstruction Network

To achieve efficient translation of  $B_z$  images, the physical knowledge is embedded into the Pix2Pix [32]. The network consists of a generator network and the discriminator network, as shown in Fig. 13. The generator network is used to generate the image of the defect according to the corresponding  $B_z$  image, and the discriminator network is used to judge the authenticity of the generated defect images. The generator network adopts the U-net structure, which is originally applied to medical image segmentation. The net uses eight downsampling layers and eight upsampling layers to extract features from images. The adjacent pixels of the  $B_z$  image are related to each other. In order to expand the receptive field of the convolution kernel, a convolution kernel with a size of 10\*10 and a stride of 1 is set to extract the deep features of the image. The max pooling module is removed to avoid missing features of the  $B_z$  image. The sampling layer adopts a fully convolutional network structure, the first upsampling layer includes convolution and activation functions, and the remaining seven downsampling layers include convolution, normalization, and activation functions. Each activation function in the downsampling module adopts LeakyReLU. The network uses batch normalization (BN) to improve the generalization. After eight downsampling layers, the image size becomes 128\*28\*28. In order to maintain the consistency of the image size, the eight upsampling layers also use a deconvolution operation with a convolution kernel size of 10 and a stride of 1. Through skip connection, the image features after each upsampling and downsampling are fused and output so that the low-level structural information and high-level semantic features of the image can be fully utilized. The first

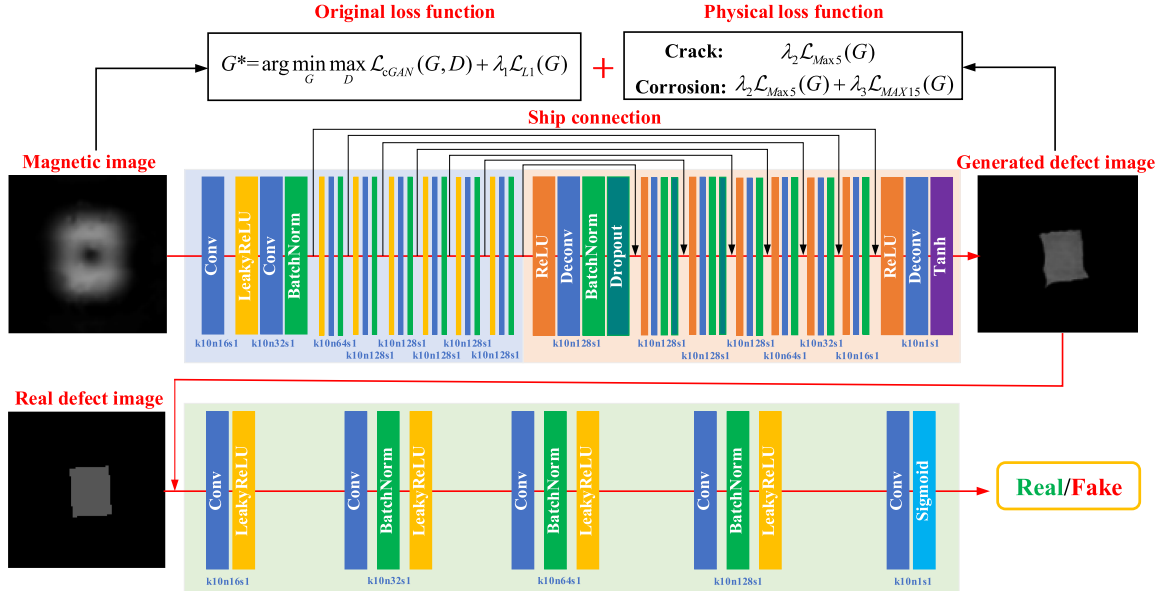


Fig. 13. Network structure.

seven activation layers of the upsampling use the ReLU, and the last layer uses the tanh. The discriminator network consists of five convolutional layers. The input layer is a convolutional layer with 16 convolution kernels, a size of  $10 \times 10$ , and a stride of 1. After the convolution operation, the LeakyReLU activation function is used. The output layer is a convolutional layer with 16 convolution kernels, a size of  $10 \times 10$ , and a stride of 1, and the activation function is the sigmoid. The middle of the network includes three downsampling operations. The number of channels will be doubled after each downsampling. The downsampling operation is a convolutional layer with a convolution kernel of  $10 \times 10$  and a stride of 1. After the convolution operation, BN is performed, and the activation function is the LeakyReLU. The dropout is added in the downsampling layers to prevent the network from overfitting, and the dropout coefficient is set to 0.5.

### C. Loss Function and Network Training

In order to obtain the best results for the reconstruction of defect 3-D contour, loss functions and training methods based on physical information are applied. First, the shape characteristics of cracks and corrosion are quite different, and the indicators for their evaluation in the field of NDT are also different. Therefore, defects are first identified and classified and then reconstructed in 3-D according to the defect types. Second, the original loss function did not take evaluation indicators into account, such as depths of cracks and corrosion. In the case of a small number of samples, modifying the loss function by adding the evaluation indicators of defects is an effective method to improve the defect reconstruction accuracy, which allows the network to optimize in the direction of physical constraints.

**1) Corrosion Loss Function:** For corrosion, the maximum depth and the volume are important indicators for evaluating the degree of corrosion, which are crucial for the safety assessment

of equipment. The presence of large deviation pixels in the generated corrosion relative to the actual corrosion results in a large maximum depth error. The  $\mathcal{L}_{\text{Max5}}$  is proposed to constrain the maximum pixel value of the generated image for the accurate maximum depth results, which takes the five-point average to reduce the influence of random errors on the results. In order to obtain a more accurate defect volume, the  $\mathcal{L}_{\text{MAX15}}$  is added to the loss function, which makes the generated corrosion contours closer to the actual corrosion by increasing the weight of the 15 pixels with the largest deviation.

For corrosion, our final loss function formula is as follows:

$$\begin{aligned} G^* = & \arg \min_G \max_D \mathcal{L}_{cGAN}(G, D) + \lambda_1 \mathcal{L}_{L1}(G) \\ & + \lambda_2 \mathcal{L}_{\text{Max5}}(G) + \lambda_3 \mathcal{L}_{\text{MAX15}}(G). \end{aligned} \quad (6)$$

$G$  tries to minimize this objective against an adversarial  $D$  that tries to maximize it.  $\lambda_1$ ,  $\lambda_2$ , and  $\lambda_3$  are the weighting factors.  $\mathcal{L}_{cGAN}$  and  $\mathcal{L}_{L1}$  are shown as follows:

$$\begin{aligned} \mathcal{L}_{cGAN}(G, D) = & \mathbb{E}_{x,y} [\log D(x, y)] \\ & + \mathbb{E}_{x,z} [\log(1 - D(x, G(x, z)))] \end{aligned} \quad (7)$$

$$\mathcal{L}_{L1}(G) = \mathbb{E}_{x,y,z} [||y - G(x, z)||_1] \quad (8)$$

where  $x$  is the  $Bz$  image,  $y$  is the defect image, and  $z$  is the random noise vector.

The calculation of  $\mathcal{L}_{\text{Max5}}$  is as follows:

- 1) **Step 1:** Both the real defect images ( $100 \times 100$ ) and the generated defect images ( $100 \times 100$ ) are converted into one column array with the size of 10 000, respectively, then sort values in the array from largest to smallest.
- 2) **Step 2:** After obtaining the two arrays with the size of  $1 \times 10\,000$  from the real defect image and the generated defect image, we select the top five elements in each array to form the new array  $A$  and  $B$ , respectively. Finally, we

compute the  $\mathcal{L}_{\text{Max5}}$  through the following formula:

$$\mathcal{L}_{\text{Max5}} = \frac{1}{5} \sum_{i=1}^5 |A_i - B_i| \quad (9)$$

where  $A_i$  is the  $i$ th element in  $A$ ,  $B_i$  is the same as  $A_i$ , and  $|\cdot|$  is the absolute operation.

The calculation process of  $\mathcal{L}_{\text{MAX15}}$  is as follows:

- 1) *Step 1:* The discrepancy between the real defect image and the generated defect image is computed by

$$V = y - G(x, z) \quad (10)$$

where  $y \in R^{100 \times 100}$  is the real defect image,  $G(x, z) \in R^{100 \times 100}$  is the generated image,  $x$  is the  $Bz$  image, and  $z$  is the random noise vector. We perform an absolute operation on each element in  $V \in R^{100 \times 100}$ , and it can be represented as follows:

$$V' = \text{abs}(V_{i,j}), \quad i = 1, 2, \dots, 100, \quad j = 1, 2, \dots, 100 \quad (11)$$

where  $V_{i,j}$  is the element at the  $i$ th row and  $j$ th column in  $V$ .

- 2) *Step 2:*  $V'$  is further stretched to an array with the size of  $1 \times 10,000$ . We select the largest 15 elements in the array to form a new array denoted as  $C \in R^{1 \times 15}$ . Then, we compute the average value of  $C$  with the following formula:

$$\mathcal{L}_{\text{MAX15}} = \frac{1}{15} \sum_{i=1}^{15} C_i \quad (12)$$

where  $C_i$  is the  $i$ th element in  $C$ .

2) *Crack Loss Function:* For cracks, the depth and length are important indicators for evaluating the degree of crack. However, the difference between crack and corrosion is that the volume is not an evaluation indicator for crack due to its narrow width. So, the loss function of the final definition of the crack is as follows:

$$G* = \arg \min_G \max_D \mathcal{L}_{\text{cGAN}}(G, D) + \lambda_1 \mathcal{L}_{L1}(G) + \lambda_2 \mathcal{L}_{\text{Max5}}(G). \quad (13)$$

3) *Network Training:* Network training and hyperparameter settings are important factors to improve network performance. The Adam optimizer is selected, which requires less memory and computes different adaptive learning rates for different parameters. The training of the network is divided into two stages. In the first stage, the loss function is set to (14), the learning rate is set to 1e-4, the batch size is set to 50, the epoch is set to 150, and the optimal solution is taken. In the second stage, the loss function is set to (6) or (13), respectively, and then the learning rate is set to 1e-5, the batch size is set to 50, the epoch is set to 150, and the optimal solution is taken.

$$G* = \arg \min_G \max_D \mathcal{L}_{\text{cGAN}}(G, D) + \lambda_1 \mathcal{L}_{L1}(G). \quad (14)$$

#### D. Results and Discussion

First, the 3-D reconstruction results of corrosion are evaluated, and 15 samples in the validation set are input into the trained

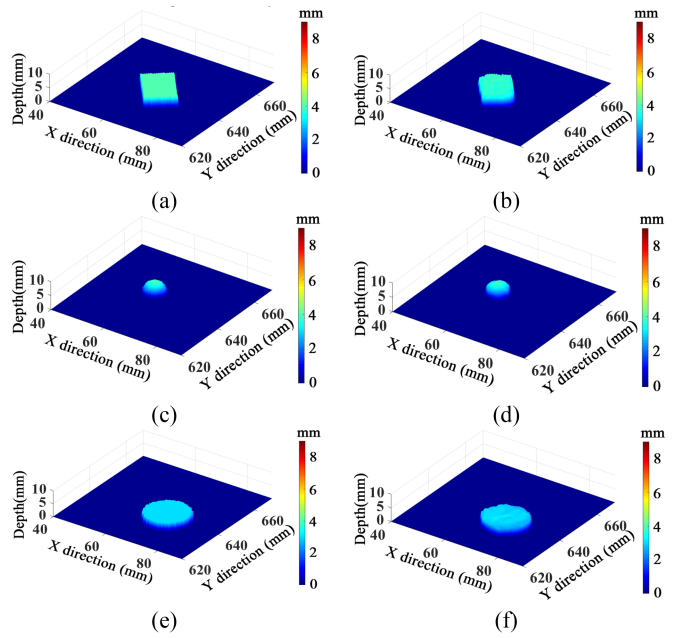


**Fig. 14.** Three-dimensional reconstruction results of corrosion defects. (a) Real rectangular corrosion. (b) Generated rectangular corrosion. (c) Real spherical corrosion. (d) Generated spherical corrosion. (e) Real cylindrical corrosion. (f) Generated cylindrical corrosion.

**TABLE III**  
CORROSION RECONSTRUCTION RESULTS FOR DIFFERENT METHODS

Data Set	Loss function	Depth error(mm)	Volume error
Co	$\mathcal{L}_{\text{cGAN}} + \mathcal{L}_{L1}$	1.3962	0.0691
	$\mathcal{L}_{\text{cGAN}} + \mathcal{L}_{L1} + \mathcal{L}_{\text{Max5}} + \mathcal{L}_{\text{MAX15}}$	<b>0.3464</b>	<b>0.0667</b>
To	$\mathcal{L}_{\text{cGAN}} + \mathcal{L}_{L1}$	1.1689	0.0670
	$\mathcal{L}_{\text{cGAN}} + \mathcal{L}_{L1} + \mathcal{L}_{\text{Max5}}$	0.6164	0.1140
	$\mathcal{L}_{\text{cGAN}} + \mathcal{L}_{L1} + \mathcal{L}_{\text{Max5}} + \mathcal{L}_{\text{MAX15}}$	0.7115	0.1660

network. Different types of corrosion 3-D reconstruction results are shown in Fig. 14. It can be seen from the figure that this method can obtain good 3-D reconstruction results for rectangular, cylindrical, and spherical corrosion. In order to verify the superiority of the method proposed in this article, the results of different datasets and different loss functions are compared and analyzed. The volume and the maximum depth are the most important indicators for evaluating the degree of corrosion. The results of the 3-D reconstruction of the corrosion obtained by different methods are shown in Table III. It shows that the average maximum depth error is 0.3464 mm and the average error of the volume is 0.0667 for the corrosion reconstructed by the method proposed in this article, which is significantly better than the other methods. The maximum depth of corrosion is the average of the five deepest corrosion points. The volume error is the ratio of the difference between the real volume and the reconstructed volume to the real volume. The results of maximum depth error and volume error for 15 samples in the validation set are shown in Fig. 15. It shows that the maximum depth error is less than 1 mm and the maximum volume error

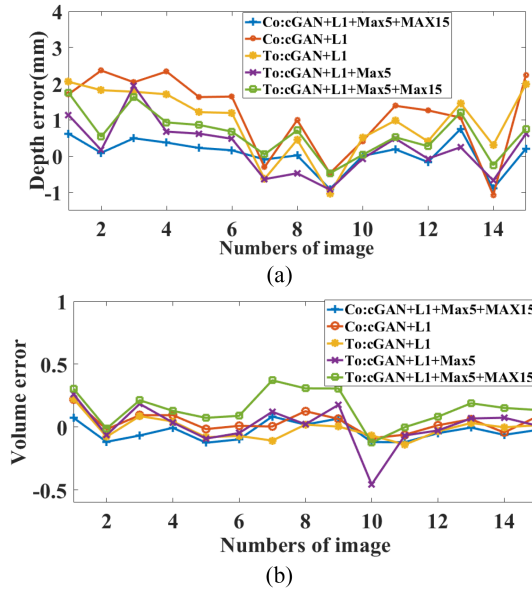


Fig. 15. Error of generated corrosion for different methods. (a) Depth error. (b) Volume error.

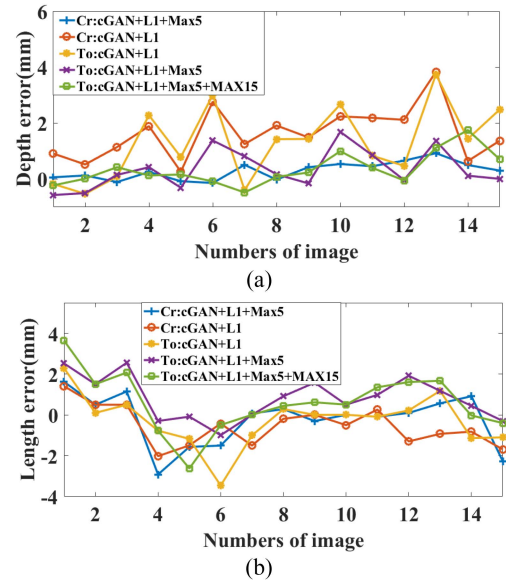


Fig. 17. Error of generated crack for different methods. (a) Depth error. (b) Length error.

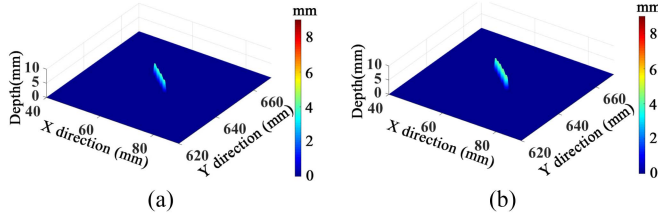


Fig. 16. Reconstruction results of crack defects. (a) Real crack. (b) Generated crack.

TABLE IV  
CRACK RECONSTRUCTION RESULTS FOR DIFFERENT METHODS

Data Set	Loss function	Depth error(mm)	Length error
Cr	$\mathcal{L}_{cGAN} + \mathcal{L}_{L1}$	1.6358	0.9022
	$\mathcal{L}_{cGAN} + \mathcal{L}_{L1} + \mathcal{L}_{Max5}$	<b>0.3402</b>	<b>0.9249</b>
To	$\mathcal{L}_{cGAN} + \mathcal{L}_{L1}$	1.4504	0.8885
	$\mathcal{L}_{cGAN} + \mathcal{L}_{L1} + \mathcal{L}_{Max5}$	0.5694	1.0549
	$\mathcal{L}_{cGAN} + \mathcal{L}_{L1} + \mathcal{L}_{Max5} + \mathcal{L}_{MAX15}$	0.4565	1.1848

is less than 0.15 for the corrosion reconstructed by the method proposed in this article, which is also significantly better than the other methods.

In order to verify the reconstruction results of this method for cracks, 15 experimental samples in the verification set are selected to reconstruct the 3-D contour of the cracks, and the results are shown in Fig. 16. It shows that the method can realize the reconstruction of cracks. The depth and the length are the most important indicators for evaluating the degree of crack. The results of crack reconstruction obtained by different methods are shown in Table IV. The average length error is 0.9249 mm and the average depth error is 0.3402 mm for the crack reconstructed by the method proposed in this article, and the depth prediction accuracy is significantly better than other

networks. At the same time, the results of the depth error and length error of the 15 samples in the validation set are shown in Fig. 17. It can be seen from the figures that the maximum error of the crack depth is less than 1 mm, and the maximum error of the crack length is less than 3 mm, which proves that the method can achieve accurate 3-D contour reconstruction of cracks. The time to reconstruct a defect in the automatic detection system by the network is 1.738 s, which can fully meet the requirements of the inspection speed.

## V. CONCLUSION

In this article, an end-to-end physics-informed neural network for defect identification and 3-D reconstruction was proposed. First, the electromagnetic induction laws of one, two, and three coils were compared and analyzed, and detection probes for different coils were made. The detection results of cracks at different angles showed that both the probes with two and three coils have the same sensitivity to defects in any directions, but the overlapping area of the three coils is smaller. The system of the two coils is simple, and the error in the detection results is smaller. A high-precision automatic defect detection system was established, and it includes a robotic arm motion system, an RACFM system, and a collaborative detection software system. Second, through the established detection system and simulation model, a dataset of corrosion and cracks was established. The faster-RCNN algorithm was used to identify and classify defects. Its mAP is 0.9982, the AP for crack identification is 0.9977, and the AP for corrosion identification is 0.9987. Finally, paired  $B_z$  images and defect databases were built. The physics-informed Pix2Pix network was proposed to realize the translation of  $B_z$  images into 3-D contours of defects. Loss functions based on defect evaluation indicators were constructed, and corrosion and cracks were reconstructed separately. The results showed that the average maximum depth error of corrosion is 0.3464 mm, the average volume error of corrosion is 0.0667, the average

depth error of cracks is 0.3402 mm, and the average length error of cracks is 0.9249 mm. These results demonstrate that the method proposed in this article realizes the defect intelligent identification and 3-D reconstruction for electromagnetic NDT technology.

Due to the difficulty in obtaining industrial field defects, the types and quantities of defect samples in this article are of a limited variety. Only a few typical defects are selected, and they are all open-type defects, and subsurface defects are not considered. In the future, more types of defects, such as subsurface defects, will be added to the dataset, and 3-D reconstruction of complex defects will be performed.

## REFERENCES

- [1] H. Liu, C. Pei, S. Xie, Y. Li, Y. Zhao, and Z. Chen, "Inversion technique for quantitative infrared thermography evaluation of delamination defects in multilayered structures," *IEEE Trans. Ind. Inform.*, vol. 16, no. 7, pp. 4592–4602, Jul. 2020, doi: [10.1109/TII.2019.2950808](https://doi.org/10.1109/TII.2019.2950808).
- [2] G. Ru, B. Gao, D. Liu, Q. Ma, H. Li, and W. L. Woo, "Structural coupled electromagnetic sensing of defects diagnostic system," *IEEE Trans. Ind. Electron.*, vol. 70, no. 1, pp. 951–964, Jan. 2023, doi: [10.1109/TIE.2022.3148755](https://doi.org/10.1109/TIE.2022.3148755).
- [3] F. Elischberger, J. Bamberg, and X. Jiang, "Deep-learning-based detection of segregations for ultrasonic testing," *IEEE Trans. Instrum. Meas.*, vol. 71, pp. 1–16, 2022, doi: [10.1109/TIM.2022.3144728](https://doi.org/10.1109/TIM.2022.3144728).
- [4] M. Fu, J. Liu, H. Zhang, and S. Lu, "Multisensor fusion for magnetic flux leakage defect characterization under information incompleteness," *IEEE Trans. Ind. Electron.*, vol. 68, no. 5, pp. 4382–4392, May 2021, doi: [10.1109/TIE.2020.2984444](https://doi.org/10.1109/TIE.2020.2984444).
- [5] A. Glowacz, "Thermographic fault diagnosis of ventilation in BLDC motors," *Sensors*, vol. 21, no. 21, 2021, Art. no. 7245, doi: [10.3390/s21217245](https://doi.org/10.3390/s21217245).
- [6] A. Glowacz, "Ventilation diagnosis of angle grinder using thermal imaging," *Sensors*, vol. 21, no. 8, 2021, Art. no. 2853, doi: [10.3390/s21082853](https://doi.org/10.3390/s21082853).
- [7] Q. Yi, H. Malekmohammadi, G. Y. Tian, S. Laureti, and M. Ricci, "Quantitative evaluation of crack depths on thin aluminum plate using eddy current pulse-compression thermography," *IEEE Trans. Ind. Inform.*, vol. 16, no. 6, pp. 3963–3973, Jun. 2020, doi: [10.1109/TII.2019.2943669](https://doi.org/10.1109/TII.2019.2943669).
- [8] J. Zhu et al., "Characterization of rolling contact fatigue cracks in rails by eddy current pulsed thermography," *IEEE Trans. Ind. Inform.*, vol. 17, no. 4, pp. 2307–2315, Apr. 2021, doi: [10.1109/TII.2020.3003335](https://doi.org/10.1109/TII.2020.3003335).
- [9] M. Nandy, B. B. Lahiri, and J. Philip, "Magnetic nanoemulsion aided optical defect detection in carbon steel components: Effect of defect width variation on optical contrast," *J. Appl. Phys.*, vol. 131, no. 20, 2022, Art. no. 204702, doi: [10.1063/5.0088554](https://doi.org/10.1063/5.0088554).
- [10] C. Ye, N. Zhang, L. Peng, and Y. Tao, "Flexible array probe with in-plane differential multichannels for inspection of microdefects on curved surface," *IEEE Trans. Ind. Electron.*, vol. 69, no. 1, pp. 900–910, Jan. 2022, doi: [10.1109/TIE.2021.3050376](https://doi.org/10.1109/TIE.2021.3050376).
- [11] J. Ge, B. Hu, and C. Yang, "Investigation of the approximate decomposition of alternating current field measurement signals from crack colonies," *Mech. Syst. Signal Process.*, vol. 160, 2021, Art. no. 107878, doi: [10.1016/j.ymssp.2021.107878](https://doi.org/10.1016/j.ymssp.2021.107878).
- [12] J. Shen et al., "Analysis on asymmetrical RCF cracks characterisation using an ACFM sensor and the influence of the rail head profile," *Measurement*, vol. 194, 2022, Art. no. 111008, doi: [10.1016/j.measurement.2022.111008](https://doi.org/10.1016/j.measurement.2022.111008).
- [13] Z. Wu, G. Dai, G. Zhou, and J. Leng, "The measurement to the pillar fillet weld of the differential settlement spherical tank by the ACFM," *IOP Conf. Ser. Mater. Sci. Eng.*, vol. 772, no. 1, 2020, Art. no. 012070, doi: [10.1088/1757-899X/772/1/012070](https://doi.org/10.1088/1757-899X/772/1/012070).
- [14] W. Li, X. Yuan, G. Chen, J. Ge, X. Yin, and K. Li, "High sensitivity rotating alternating current field measurement for arbitrary-angle underwater cracks," *NDT&E Int.*, vol. 79, pp. 123–131, 2016, doi: [10.1016/j.ndteint.2016.01.003](https://doi.org/10.1016/j.ndteint.2016.01.003).
- [15] N. Zhang, C. Ye, L. Peng, and Y. Tao, "Eddy current probe with three-phase excitation and integrated array tunnel magnetoresistance sensors," *IEEE Trans. Ind. Electron.*, vol. 68, no. 6, pp. 5325–5336, Jun. 2021, doi: [10.1109/TIE.2020.2989704](https://doi.org/10.1109/TIE.2020.2989704).
- [16] C. Ye, Y. Huang, L. Udupa, and S. S. Udupa, "Novel rotating current probe with GMR array sensors for steam generate tube inspection," *IEEE Sensors J.*, vol. 16, no. 12, pp. 4995–5002, Jun. 2016, doi: [10.1109/JSEN.2016.2556221](https://doi.org/10.1109/JSEN.2016.2556221).
- [17] X. Yin et al., "Detection of outer wall defects on steel pipe using an encircling rotating electromagnetic field eddy current (RoFEC) technique," *Slovenski vestnik - J. Mech. Eng.*, vol. 68, no. 1, pp. 27–38, 2022, doi: [10.5545/sv-jme.2021.7288](https://doi.org/10.5545/sv-jme.2021.7288).
- [18] X. Yuan et al., "Identification of tiny surface cracks in a rugged weld by signal gradient algorithm using the ACFM technique," *Sensors*, vol. 20, no. 2, 2020, Art. no. 380, doi: [10.3390/s20020380](https://doi.org/10.3390/s20020380).
- [19] L. Sun, S. Zhao, Y. Shen, J. Wang, and J. Gao, "A performance improved ACFM-TMR detection system with tradeoff denoising algorithm," *J. Magnetism Magn. Mater.*, vol. 527, 2021, Art. no. 167756, doi: [10.1016/j.jmmm.2021.167756](https://doi.org/10.1016/j.jmmm.2021.167756).
- [20] S. Zhao, L. Sun, J. Gao, J. Wang, and Y. Shen, "Uniaxial ACFM detection system for metal crack size estimation using magnetic signature waveform analysis," *Measurement*, vol. 164, 2020, Art. no. 108090, doi: [10.1016/j.measurement.2020.108090](https://doi.org/10.1016/j.measurement.2020.108090).
- [21] X. Yuan, W. Li, G. Chen, X. Yin, W. Yang, and J. Ge, "Two-step interpolation algorithm for measurement of longitudinal cracks on pipe strings using circumferential current field testing system," *IEEE Trans. Ind. Inform.*, vol. 14, no. 2, pp. 394–402, Feb. 2018, doi: [10.1109/TII.2017.2728804](https://doi.org/10.1109/TII.2017.2728804).
- [22] S. Zhao et al., "Extreme learning machine based sub-surface crack detection and quantification method for ACFM," *J. Magnetism Magn. Mater.*, vol. 546, 2022, Art. no. 168865, doi: [10.1016/j.jmmm.2021.168865](https://doi.org/10.1016/j.jmmm.2021.168865).
- [23] D. J. Pasadas, A. L. Ribeiro, H. G. Ramos, and T. J. Rocha, "Inspection of cracks in aluminum multilayer structures using planar ECT probe and inversion problem," *IEEE Trans. Instrum. Meas.*, vol. 66, no. 5, pp. 920–927, May 2017, doi: [10.1109/TIM.2017.2682758](https://doi.org/10.1109/TIM.2017.2682758).
- [24] D. J. Pasadas, A. L. Ribeiro, T. Rocha, and H. G. Ramos, "2D surface defect images applying Tikhonov regularized inversion and ECT," *NDT&E Int.*, vol. 80, pp. 48–57, 2016, doi: [10.1016/j.ndteint.2016.02.009](https://doi.org/10.1016/j.ndteint.2016.02.009).
- [25] X. Yuan et al., "Visual and intelligent identification methods for defects in underwater structure using alternating current field measurement technique," *IEEE Trans. Ind. Inform.*, vol. 18, no. 6, pp. 3853–3862, Jun. 2022, doi: [10.1109/TII.2021.3117034](https://doi.org/10.1109/TII.2021.3117034).
- [26] A. Noroozi, R. P. R. Hasanzadeh, and M. Ravan, "A fuzzy learning approach for identification of arbitrary crack profiles using ACFM technique," *IEEE Trans. Magn.*, vol. 49, no. 9, pp. 5016–5027, Sep. 2013, doi: [10.1109/TMAG.2013.2254718](https://doi.org/10.1109/TMAG.2013.2254718).
- [27] L. Yang, Z. Wang, and S. Gao, "Pipeline magnetic flux leakage image detection algorithm based on multiscale SSD network," *IEEE Trans. Ind. Inform.*, vol. 16, no. 1, pp. 501–509, Jan. 2020, doi: [10.1109/TII.2019.2926283](https://doi.org/10.1109/TII.2019.2926283).
- [28] B. Du, Y. He, Yunze He, J. Duan, and Y. Zhang, "Intelligent classification of silicon photovoltaic cell defects based on eddy current thermography and convolution neural network," *IEEE Trans. Ind. Inform.*, vol. 16, no. 10, pp. 6242–6251, Oct. 2020, doi: [10.1109/TII.2019.2952261](https://doi.org/10.1109/TII.2019.2952261).
- [29] C. Y. Wang et al., "YOLOv7: Trainable bag-of-freebies sets new state-of-the-art for real-time object detectors," 2022, doi: [10.48550/arXiv.2207.02696](https://arxiv.org/abs/2207.02696).
- [30] W. Liu et al., "SSD: Single shot multibox detector," in *Proc. Eur. Conf. Comput. Vis.*, 2016, pp. 21–37, doi: [10.1007/978-3-319-46448-0\\_2](https://doi.org/10.1007/978-3-319-46448-0_2).
- [31] S. Ren, K. He, R. Girshick, and J. Sun, "Faster R-CNN: Towards real-time object detection with region proposal networks," *IEEE Trans. Pattern Anal. Mach. Intell.*, vol. 39, no. 6, pp. 1137–1149, Jun. 2017, doi: [10.1109/TPAMI.2016.2577031](https://doi.org/10.1109/TPAMI.2016.2577031).
- [32] P. Isola, J.-Y. Zhu, T. Zhou, and A. A. Efros, "Image-to-image translation with conditional adversarial networks," in *Proc. IEEE Conf. Comput. Vis. Pattern Recognit.*, 2017, pp. 5967–5976, doi: [10.1109/CVPR.2017.632](https://doi.org/10.1109/CVPR.2017.632).



**Jianming Zhao** received the B.E. degree in mechanical design manufacture and automation in 2017 from the China University of Petroleum (East China), Qingdao, China, where he is currently working toward the Ph.D. degree in mechanical engineering.

His research interests include signal processing, inversion imaging, and deep learning.



**Wei Li** (Member, IEEE) received the Ph.D. degree in mechanical and electronics engineering from the China University of Petroleum (East China), Qingdao, China, in 2007.

Following graduation, he joined the China University of Petroleum (East China), where he is currently a Professor of mechanical and electronics engineering. His current research interests include electromagnetic nondestructive evaluation and signal processing, offshore engineering structure design and finite-element method analysis, and pipeline safety and reliability assessment.



**Xin'an Yuan** was born in Nanyang, China, on March 12, 1990. He received the B.E., M.E., and Ph.D. degrees in mechanical design manufacture and automation from the China University of Petroleum (East China), Qingdao, China, in 2013, 2016, and 2019, respectively.

Following graduation, he joined the China University of Petroleum (East China), where he is currently an Associate Professor with the Research Institute of Center for Offshore Engineering and Safety Technology. His research interests include nondestructive testing, signal processing, and deep learning.



**Xiaokang Yin** (Senior Member, IEEE) received the B.E. degree in information engineering from the East China University of Science and Technology, Shanghai, China, in 2005, and the M.S. degree in advanced electronic engineering and the Ph.D. degree in engineering from the University of Warwick, Coventry, U.K., in 2007 and 2011, respectively.

In 2011, he joined the China University of Petroleum (East China), Qingdao, China, where he is currently a Professor of mechanical and electronic engineering.



**Xiao Li** received the Ph.D. degree in mechanical engineering from the Dalian University of Technology, Dalian, China, in 2019.

He is currently a Lecturer with the China University of Petroleum (East China), Qingdao, China. His research interests include machine vision and contouring detection for machine tools.



**Qinyu Chen** received the B.E. degree in mechanical design manufacture and automation in 2021 from the China University of Petroleum, Qingdao, China, where he is currently working toward the M.E. degree in mechanical engineering.

His research interests include model analysis.



**Jianxi Ding** received the B.E. degree in mechanical design manufacture and automation in 2020 from the China University of Petroleum, Qingdao, China, where he is currently working toward the Ph.D. degree in mechanical engineering.

His research interests include deep learning.